Materials & Design 242 (2024) 113028

Contents lists available at ScienceDirect

Materials & Design

journal homepage: www.elsevier.com/locate/matdes

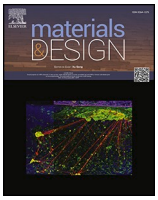

Strain hardening behavior in T-carbon: A molecular dynamics study

Runhua Zhou [a,b], Lichun Bai [c], Changjin Huang [a], Narasimalu Srikanth [b], Mao See Wu [a,*]

[a] School of Mechanical and Aerospace Engineering, Nanyang Technological University, 639798, Singapore
[b] Energy Research Institute, Nanyang Technological University, 637141, Singapore
[c] Key Laboratory of Traffic Safety on Track (Central South University), Ministry of Education, School of Traffic and Transportation Engineering, Central South University, Changsha 410075, China

ARTICLE INFO

Keywords:
T-carbon
Strain hardening
Molecular dynamics simulation
Ductility
Mechanical strength

ABSTRACT

T-carbon, a new carbon allotrope essentially composed of intra-tetrahedron bonds and inter-tetrahedron bonds, has attracted strong scientific interest in recent years due to its excellent mechanical performance for a wide range of applications. This study demonstrates that strain hardening can endow T-carbon with exceptional mechanical strength at a high compressive strain under plastic deformation, which is rarely observed in conventional carbon-based materials. Molecular dynamics simulations reveal that this behavior occurs in T-carbon nanowires and is caused by graphitization, where their original sp^3-dominated carbon network transforms into a stronger sp^2-network. Further analysis shows that graphitization occurs due to the breaking of intra-tetrahedron bonds, which is dominated by the deformation behavior of inter-tetrahedron bond angles. Particularly, when the deformation angle is small, only a small portion of the strain energy is stored in the tetrahedrons, while the remaining energy is released by breaking the intra-tetrahedron bonds of T-carbon nanowires, thus leading to graphitization. Moreover, such underlying mechanisms behind strain hardening and graphitization are found to occur in bulk T-carbon. This strain hardening potentially enables T-carbon to overcome the strength–ductility tradeoff issue of high strength leading to ductility loss.

1. Introduction

The strength–ductility tradeoff is a fundamental concept in materials science and engineering, playing a crucial role in the design and selection of suitable structural materials for various applications [1,2]. High-strength materials offer exceptional resistance to deformation and failure under applied loads, making them desirable for applications that require strong load-bearing capacity. However, these materials typically possess a dense atomic structure, which impedes the motion of atoms and makes it difficult for the materials to undergo strain hardening. As a result, they tend to exhibit lower ductility and are more likely to fracture or fail under stress without significant plastic deformation [3–5]. Researchers and engineers have employed various techniques, such as microstructural control [6,7], mechanical treatment [8,9], and heat treatment [10,11], to overcome the inherent strength–ductility tradeoff and customize materials. Nevertheless, scaling up these advancements for the cost-effective production of industrial parts remains a significant challenge.

Carbon-based materials have garnered significant research attention in recent decades owing to their exceptional mechanical properties. The ductility and strength of such materials are primarily dictated by their crystal structure and atomic bonding. Certain carbon-based materials, like diamond and lonsdaleite, are composed of strong covalent bonds and exhibit highly ordered crystal structures. However, they lack ductility due to their rigid structure and strong covalent bonds, which impede the movement of dislocations and hinder plastic deformation [12,13]. On the other hand, some carbon-based materials consist predominantly of amorphous carbon, such as diamond-like carbon and glassy carbon, which lack long-range order and possess disordered crystal structures. These materials possess nonhomogeneous density and localized strain, which make them more susceptible to brittle fracture [14,15]. Furthermore, highly porous carbon-based materials, including carbon aerogels and carbon foam, have large surface areas and low densities. They also contribute to a fragile structure due to the interconnected network of carbon particles [16,17]. Consequently, these carbon-based materials lack the ability to withstand stress through plastic deformation.

T-carbon is a new carbon allotrope, and its structure was first proposed through theoretical calculations [18]. The unique configuration of T-carbon resembles that of diamond, albeit with each carbon atom

* Corresponding author.
E-mail address: mmswu@ntu.edu.sg (M. See Wu).

https://doi.org/10.1016/j.matdes.2024.113028
Received 27 February 2024; Received in revised form 15 May 2024; Accepted 15 May 2024
Available online 16 May 2024

substituted by a tetrahedral unit consisting of four sp^3-hybridized carbon atoms. T-carbon nanowires (NWs) were fabricated via the exposure of multi-walled carbon nanotubes, which were dissolved in a solution of methanol, to a high-energy picosecond laser [19]. Subsequently, bulk T-carbon was also fabricated through a plasma-enhanced chemical vapor deposition technique, utilizing polycrystalline and single-crystalline diamond substrates [20].

In the recent years, T-carbon has found important applications in ion batteries [21,22], photocatalysts [23], electrocatalysts [24], optoelectronic detectors [25], irradiation resistance devices [26], topological phonons [27], and magnetism and superconductivity [28]. However, the mechanical properties of T-carbon remain largely unexplored. From a structural perspective, T-carbon possesses large spacings between its constituent carbon atoms, resulting in a lower density compared to graphite and diamond. Because of these structural characteristics, T-carbon may exhibit excellent plastic deformability [29]. It is important to explore the structural evolution of T-carbon during plastic deformation, including the deformation of bonds, bond angles, and tetrahedrons.

This work is devoted to investigating the mechanisms of plastic deformation and strain hardening behaviors in T-carbon under compressive loading using molecular dynamics (MD) simulations. MD is a computational method that simulates the evolution of molecular systems over time. By simulating the movement of atoms and molecules, it can reveal the structure, dynamic properties, and thermodynamic behavior of materials, thereby providing a basis for understanding and designing molecular-level processes to provide important insights. MD simulations can be relatively cost-effective while conducting experiments can be expensive and time-consuming [30]. They can also complement experimental work and reduce the need for extensive trial-and-error experimentation. Key considerations are given to factors such as the lattice orientation and radius of T-carbon NWs. The structural evolution of T-carbon NWs during deformation is analyzed, and the correlation between the deformation of tetrahedrons and strain hardening mechanisms in NWs is established and validated in bulk T-carbon.

2. Modeling

MD simulation is conducted to study the mechanical properties of T-carbon structure subjected to compressive deformation along different lattice orientations (Fig. 1a). All simulations are performed using the software Large-scale Atomic/Molecular Massively Parallel Simulator (LAMMPS) [31], which has proven to be a powerful tool for providing nanoscale-level understanding of the mechanical behavior and deformation mechanisms of carbon-based materials [32].

The adaptive intermolecular reactive empirical bond order (AIREBO) potential is used to characterize the interaction between carbon atoms and has shown excellent accuracy in studying various carbon-based materials [14,33], especially T-carbon [34]. The default cutoff parameter settings are used in our simulations [35], which have been proven to represent the excellent mechanical properties of T-carbon in previous studies [34]. It is known that covalent bonding plays a dominant role in determining the mechanical performance of carbon-based materials. In addition, it is found that the non-covalent interactions exert negligible influence on the mechanical properties of carbon-based materials [36]. Therefore, the non-covalent interactions in the AIREBO potential are not considered in order to save on computational cost. The software Open Visualization Tool (OVITO) is used to visualize the simulation results [37].

T-carbon exhibits a distinct lattice structure and atomic arrangement that set it apart from diamonds. A unit cell of T-carbon is initially built according to its reported structure in a previous work [18], as shown in Fig. 1b. The lattice constant of the unit cell is obtained as 7.9 Å, consistent with the experimental value (~7.8 Å) [20]. Before modeling, the unit cell is relaxed at 10 K and 0 kPa with an isothermal-isobaric (NPT) ensemble in three-dimensional periodic boundary conditions for 10 ps to release internal strains [38].

Then, the unit cell of T-carbon is duplicated to prepare NWs with different radii (35, 50, and 65 Å) and a length of ~ 210 Å, based on experimental observations [19], as well as bulk T-carbon samples. The longitudinal orientations of the NWs are aligned with various lattice orientations (Fig. 1c–e). The lateral dimensions of all bulk samples are set to ~ 100 Å.

The compressive deformation of T-carbon NWs and bulk T-carbon is evaluated by assessing the bonding states of the constituent atoms using the atomic coordinate number (CN) with a cutoff radius of 1.95 Å, a distance that corresponds to the first minimum location in the radial distribution function. The values of CN can be used to describe the types of bonds formed by the atoms, with CN = 4, 3, and 2 indicating sp^3, sp^2, and sp bonding states, respectively. More information about the calculation of CN can be found in earlier works [39,40].

Compressive simulations are commonly realized using the incremental strain loading method, as described in the literature [41]. In a previous work, the incremental loading method was proven feasible for studying the tensile properties of T-carbon NWs [34]. Hence, this method is utilized in this research to study the compressive properties of T-carbon NWs.

The two ends of the T-carbon NW are set as rigid layers, each layer has a length of 20 Å, and the middle movable layer has a length of 170 Å. One layer is set to be static, and the other layer is compressed along the Y-axis direction. This requires the NWs to have boundary conditions that are non-periodic and shrink-wrapped in all directions. The time step is set to 0.001 ps. Before compressive loading, the movable layer is relaxed

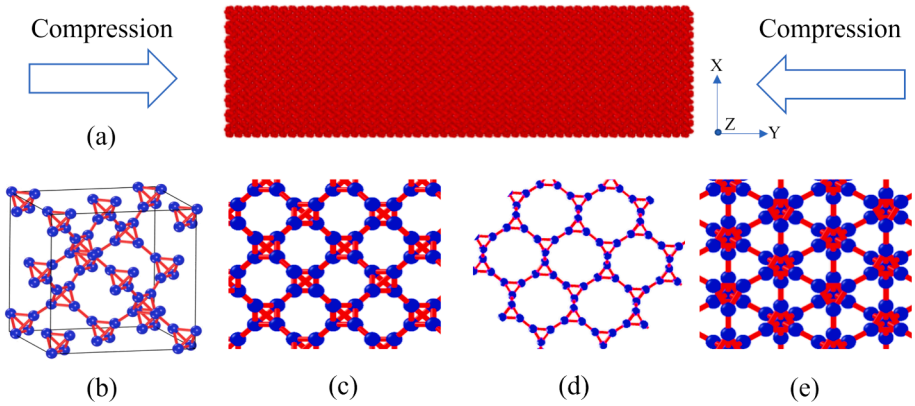

Fig. 1. Simulation cells and the various lattice orientations considered in the present work. (a) Illustration of the MD simulation model for performing compressive testing. (b) The cubic crystal lattice of T-carbon resulting from the replacement of each carbon atom in a diamond with a tetrahedron carbon unit. (c)–(e) Views from the [1 0 0], [1 1 0], and [1 1 1] orientations of T-carbon, respectively.

by the isothermal-isochoric (NVT) ensemble for 18 ps and the temperature is set to 300 K. The incremental loading involves step-wise strain increments with system relaxation at each step [42]. After each incremental increase in strain, which occurs over a duration of 1 ps, a subsequent period of static relaxation follows, lasting for 5 ps. The incremental loading occurs 600 times in total, and the movable distance of each loading is 0.17 Å. Therefore, the total deformation and total time of this simulation are 102 Å and 3600 ps, respectively. The strain rate and total strain of compressive deformation of the T-carbon NWs can be calculated as 1.67×10^{-4} / ps and 0.6, respectively. This method can simulate the fixation of the collet to the end during real compression.

During the simulation of bulk T-carbon, the unit cell uniformly shrinks along the compressive direction of bulk T-carbon with continuous strain increments [43,44]. Unlike the NWs, periodic boundary conditions are applied in all directions. Before compressive loading, the model is relaxed by the NPT ensemble for 100 ps and the total time of simulation is 5000 ps. The other conditions are the same as the NWs.

3. Results

3.1. Strain hardening behavior in T-carbon NWs

The stress–strain (σ–ε) relationships of T-carbon NWs under compressive loading are first evaluated (Fig. 2a–c). It is found that the relationships are highly dependent on the lattice orientation and cross-sectional radius (R) of the T-carbon NWs.

The strain hardening behavior is found for all T-carbon NWs under compressive loading regardless of their lattice orientations. In our work, the strain hardening behavior is identified as a noticeable increase in σ after yielding. For example, in the case of $R = 35$ Å (Fig. 2a), σ increases when $\varepsilon < 0.47$ and drops significantly in the range of $0.47 < \varepsilon < 0.48$ when the load is applied along the [1 0 0] orientation. Subsequently, when $\varepsilon > 0.48$, σ increases rapidly in a discrete manner until $\varepsilon = 0.6$.

The strain hardening behavior of T-carbon NWs can simultaneously endow this material with high mechanical strength and excellent ductility, which is rarely reported in conventional carbon-based materials. For example, when the load is applied along the [1 1 1] orientation in the case of $R = 65$ Å (Fig. 2c), the value of σ ($0.13 < \varepsilon < 0.6$) after yielding increases significantly by roughly fourfold from 6.7 to 28 GPa due to strain hardening. Compared with the simulation results of diamond NWs fractured at $\varepsilon = 0.35$ [45], T-carbon NWs can sustain further compressive loading up to strains of 0.6, indicative of their high ductility.

In addition, it is observed that σ at $\varepsilon = 0.6$ becomes higher at a larger R (Fig. 2a–c) for loading along the [1 1 0] and [1 1 1] directions. For instance, as R increases from 35 to 65 Å when the load is applied along the [1 1 0] orientation, the value of σ increases from 9 to 22 GPa at $\varepsilon = 0.6$. These findings indicate that the strain hardening behavior in T-carbon NWs is influenced by the size of the NW. Such a mechanism was confirmed in carbon-based nanomaterials through compressive experiments [46].

3.2. Evolution of the graphitization in T-carbon NWs

The strain hardening behavior of T-carbon NWs may be attributed to microstructural changes caused by compressive strains. Hence, transitions among the different atomic bonding states can be used to explain the strain hardening effect further. The transition of atoms from sp^3 to sp^2 bonding is typically defined as the graphitization process. Thus, a high sp^2 fraction (f_{sp2}) reflects a high graphitization level [26,42].

The propagation degree and speed of graphitization show different dependence on the R of T-carbon NWs in different lattice orientations (Fig. 2d–f). For the [1 1 0] orientation, the propagation degree and speed of graphitization increase most obviously with the increase of R. However, graphitization in the [1 0 0] orientation is the least sensitive to the changes in R.

For instance, along the [1 1 0] orientation, when the R increases from 35 to 65 Å, f_{sp2} can quickly increase from 13 % to 40 % at $\varepsilon = 0.1$ (Fig. 2d-f). Moreover, the final value of f_{sp2} at fracture strain is shown to have increased from 48 % to 76 % (Fig. 2d–f). However, when the NW is

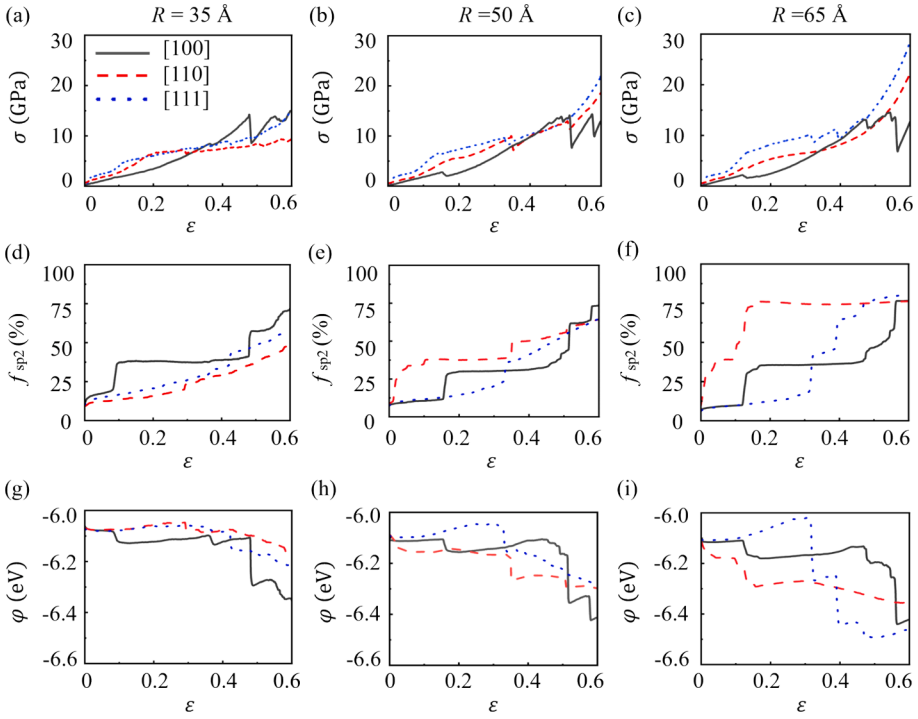

Fig. 2. Deformation responses of T-carbon NWs under compression along different lattice orientations. (a)–(c) Stress–strain (σ–ε) curves of T-carbon NWs with R equal to 35, 50, and 65 Å, respectively. (d)–(f) Evolution of the sp^2 fraction (f_{sp2}) in T-carbon NWs with R equal to 35, 50, and 65 Å, respectively. (g)–(i) Evolution of the average atomic potential (φ) in T-carbon NWs with R equal to 35, 50, and 65 Å, respectively.

loaded along the [1 0 0] orientation, the trend of f_{sp2} barely changes with respect to all R. This is attributed to the anisotropy of lattice orientations. Variations in the lattice arrangement along the loading direction result in different loading forces experienced by lattice units, thereby leading to distinct phase transitions.

The improvement in σ after a sharp increase in f_{sp2} appears to be a general trend in Fig. 2a–f. For instance, when the NW is loaded along the [1 0 0] orientation (Fig. 2a and 2d), the sharp increase of f_{sp2} when ε equals 0.47–0.48 leads to a decrease in σ, but σ continues to increase when $\varepsilon > 0.48$. The decrease in σ is due to a significant transition of carbon atoms from sp^3 to sp^2 bonding states. Experimental evidence shows that the breakage of the sp^3-dominated network can cause stress relaxation [47].

Subsequently, as ε increases, σ also rises because the newly formed sp^2-dominated network in T-carbon NWs is stronger than the original sp^3-dominated network. This phenomenon, known as graphitization, results in strain hardening in T-carbon nanowires. The correlation between f_{sp2} and σ indicates that the strain hardening mechanism of T-carbon NWs is directly related to their microstructural evolution, especially the sp^3 to sp^2 transformation.

It is worth noting that the increase in f_{sp2} always causes a decrease in σ. However, strong strain hardening occurs only when the ability of the original sp^3-dominated network to resist deformation is severely lost. Therefore, the increase of f_{sp2} along [1 0 0] orientation does not cause significant strain hardening when $\varepsilon < 0.1$ and $R = 35$ Å (Fig. 2a). Similar phenomena also appear in the other two R. Strain hardening is still observable at $R = 50$ Å ($\varepsilon = 0.15$) and $R = 65$ Å ($\varepsilon = 0.12$), respectively, although it is less obvious (Fig. 2b–c).

It is important to note that we have also performed compression tests on T-carbon NWs using higher strain rates. The results indicate that changes in strain rate do not affect the existence of strain hardening of T-carbon nanowires and that graphitization still dominates this strain hardening mechanism.

Notably, the effect of graphitization was verified in the tensile testing of T-carbon NWs [34]. Compared to the tensile loading, the graphitization only had a significant improvement along [1 1 0] and [1 1 1] lattice orientations, and the strain hardening of T-carbon NW along the [1 0 0] lattice orientation was not obviously observed. However, our simulation shows that T-carbon NWs can reach a higher graphitization level along all lattice orientations for all R under compressive deformation.

For many conventional carbon-based materials, there is always a trade-off between their strength and ductility [1,4]. For example, the ultimate compressive strength of pentadiamond was predicted as 44 GPa at $\varepsilon = \sim 0.15$ by MD simulation [36]. Upon further deformation, the newly formed carbon network in the pentadiamond was not stronger than its original sp^3–sp^2 hybridized network. As a result, a high failure strain could not be reached, resulting in a brittle fracture. In contrast, strain hardening endows T-carbon NWs with excellent ductility. This can be attributed to the formation of the sp^2-dominated network during strain hardening, which was demonstrated experimentally in some carbon-based nanomaterials [48].

In addition, the ultimate compressive strength of graphene aerogel reached less than 1.27 GPa at $\varepsilon = \sim 0.8$ in MD simulation [49]. The compressive strength of graphene aerogel was dominated by the severe deformation of graphene walls. At large strains, the graphene aerogel lost its structural stability, and its strength could not further increase, thus leading to a low fracture strength. However, the graphitization of T-carbon NWs enables the achievement of higher mechanical strength without sacrificing ductility.

It is noteworthy that graphitization may lead to changes in the potential energy of the constituent carbon atoms. Therefore, to further investigate the correlation between strain hardening and graphitization in T-carbon nanowires, the average atomic potential energy (φ) is analyzed, as illustrated in Fig. 2g–i.

The evolution of φ depends on the R of NWs when the load is applied along the [1 1 0] and [1 1 1] lattice orientations, similar to σ and f_{sp2}. For instance, when the NW has an R of 35 Å and the load is applied along the [1 1 1] orientation, φ decreases in a relatively smooth manner with a minor drop observed at $\varepsilon = \sim 0.42$ (Fig. 2g). When R is 65 Å instead, φ reduces discretely with two large drops observed at $\varepsilon = \sim 0.3$ and $\varepsilon = \sim 0.39$ (Fig. 2i). However, under compression along the [1 0 0] lattice orientation, φ evolves in a similar manner for all NWs, suggesting that there are no significant changes induced by increasing R (Fig. 2g–i).

From Fig. 2d–i, it can be seen that the changes in φ correlate well with the evolution of f_{sp2} during deformation. It is known that φ increases with ε [50,51]. However, as shown in Fig. 2d–i, an increase in f_{sp2} leads to a decrease in φ, and φ rises moderately when f_{sp2} remains relatively steady. This phenomenon arises because with increasing f_{sp2} (*i.e.*, graphitization occurs), some of the strain energy has to be absorbed in order to transform the sp^3 bonds into sp^2, thus leading to a pronounced reduction of φ. This observation demonstrates that the absorption of φ is highly related to the graphitization process of T-carbon NWs. The peculiar graphitization allows T-carbon NWs to absorb a large amount of strain energy during plastic deformation. Therefore, T-carbon holds great promise for mechanical energy-absorbing applications [52].

The graphitization process is further explored by analyzing the change of the microstructure of T-carbon NWs over time when loading is applied (Fig. 3). The [1 1 0] lattice orientation is mainly studied because graphitization is most sensitive to the change of R along this orientation. Snapshots during compression are provided to reveal the atomic details of the deformation process of T-carbon NWs.

The microstructural evolution of T-carbon NWs confirms that the propagation of graphitization highly depends on R along the [1 1 0] lattice orientation, and the sp^2-bonding region has a more pronounced expansion for larger R (Fig. 3g–i), resulting in a larger final region with sp^2-bonded atoms.

Based on a comparison between Figs. 2d–f and 3, the initial value of f_{sp2} is not equal to 0, and the surface edges of the T-carbon NWs are sp^2-bonding atoms. These sp^2-bonding atoms are caused by slicing NWs from the bulk during modeling, which act as potential graphitization areas. These surface areas initially begin to graphitize randomly when compressive strain is applied. As the ε continues to increase, graphitization gradually propagates toward the inner region of the T-carbon NWs.

As depicted in Fig. 3, graphitization primarily concentrates randomly in several regions of T-carbon NWs in the early stage of plastic deformation. With the continued increase in ε, graphitization gradually spreads uniformly from local to global. This phenomenon arises from stress concentration during buckling, which weakens as the R increases. Consequently, with an increase in R, graphitization expands more uniformly, leading to a higher degree of graphitization. This finding highlights the size effect of NWs [53,54], which can result in varying mechanical performance of the carbon network.

For traditional carbon-based materials, such as diamond-like carbon, MD simulation showed that graphitization is typically localized and does not propagate throughout the entire sp^3-dominated network during deformation, which fails to provide the material with higher resistance to deformation [55]. In comparison, the distinct phenomenon of global graphitization observed in T-carbon results in remarkable ductility. In addition, MD simulation demonstrated that the activation of graphitization of diamond-like carbon requires a high temperature to break the sp^3-dominated network [14]. However, the graphitization of T-carbon can be activated easily at room temperature.

3.3. Evolution of tetrahedral deformation in T-carbon NWs

The structural evolution of carbon tetrahedrons that make up the lattice structure of T-carbon NWs is studied to explore the nanoscale origin of graphitization. Specifically, the fraction f_{Na}, defined as the ratio of the number of tetrahedrons that fracture during compression to the total number of tetrahedrons in the undeformed NW, is monitored

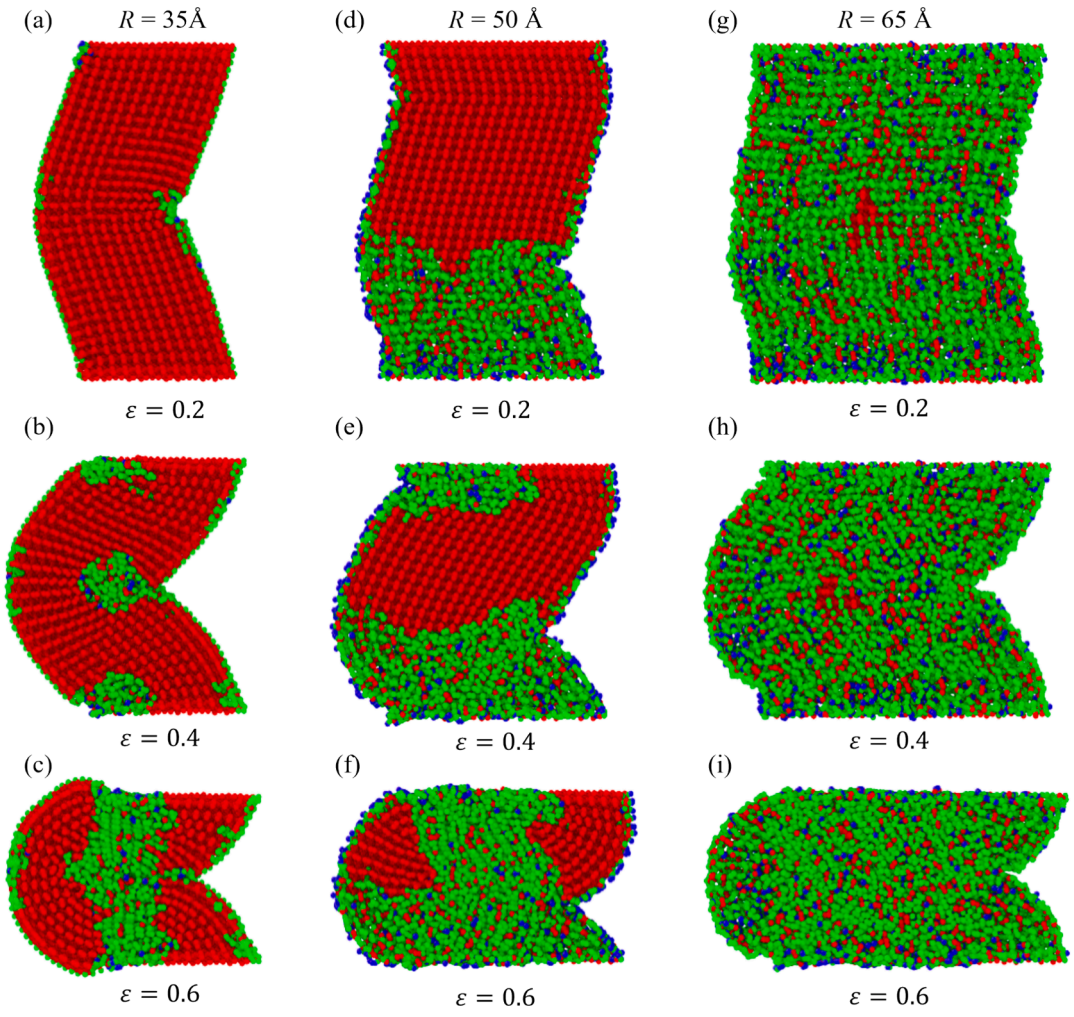

Fig. 3. Microstructural evolution of T-carbon NWs under compressive strains of $\varepsilon = 0.2$, 0.4, and 0.6 applied in the [1 1 0] lattice orientation for NWs with (a, b, c) $R = 35$ Å, (d, e, f) $R = 50$ Å, and (g, h, i) $R = 65$ Å. Red, green, and blue regions represent sp^3, sp^2, and sp bonding states, respectively.

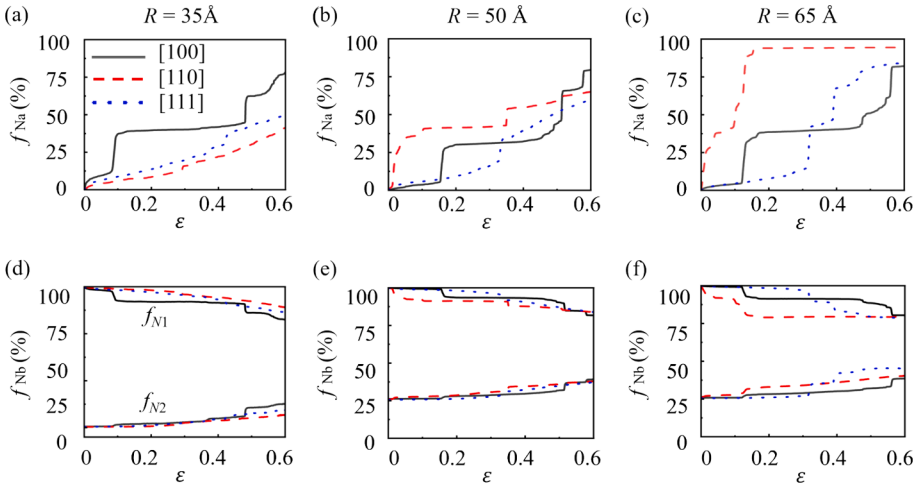

Fig. 4. Deformation responses of tetrahedrons and constituent C–C bonds of T-carbon NWs under compression along different lattice orientations. (a)–(c) Evolution of the fraction of fractured carbon tetrahedrons f_{Na} in T-carbon NWs with R equal to 35, 50, and 65 Å, respectively. (d)–(f) Evolution of the bond fraction f_{Nb} in T-carbon NWs with R equal to 35, 50, and 65 Å, respectively. f_{N1} refers to all C–C bonds in the NWs, while f_{N2} refers to the inter-tetrahedron bonds.

(Fig. 4a–c).

Based on a comparison between Figs. 2d–f and 4a–c, it can be concluded that graphitization is caused by carbon tetrahedrons fracturing under compressive strain. It is shown that the trends of f_{Na} and f_{sp2} under compressive loading are consistent with one another for all lattice orientations, although they depend on the radius R of the T-

carbon NWs. For example, it can be observed from Figs. 2f and 4c that, when $R = 65$ Å and loading is applied along the [1 1 1] lattice orientation, f_{Na} increases by ~ 25 % at $\varepsilon = -0.31$, which directly leads to an increase of ~ 20 % in f_{sp2}. Therefore, the deformation of carbon tetrahedrons highly dominates the graphitization of T-carbon NWs. This behavior arises because the intra-tetrahedron bond angle of T-carbon (60°) is much smaller than that of other sp^3 carbon materials such as diamond (109.5), resulting in an internal strain in the carbon tetrahedron structure [18]. Therefore, the unique carbon tetrahedron structure of T-carbon NWs facilitates graphitization under compression.

Further analysis indicates that the deformation of carbon tetrahedrons occurs through the breaking of its constituent carbon–carbon (C–C) bonds. By estimating the number of broken C–C bonds in the T-carbon NWs, it is shown that the transition from sp^3 to sp^2 bonding states is strongly linked to the breaking of bonds within the tetrahedrons. The fraction f_{Nb}, defined as the ratio of the number of C–C bonds remaining during compression to the total number of C–C bonds in the undeformed NW, is calculated and given in Fig. 4d–f. In addition, the C–C bonds in T-carbon NWs can be classified into two types: intra-tetrahedron bonds and inter-tetrahedron bonds [18]. The fraction f_{Nb}, can thus be further classified into f_{N1} and f_{N2}, representing the total number of C–C bonds remaining in the NW and among that, the total number of inter-tetrahedron bonds, respectively.

Fig. 4d–f show that f_{N1} decreases with increasing compressive strain in all cases, while the opposite trend is observed for f_{N2}. It can be observed from Figs. 2 and 4 that the changes in f_{N1} and f_{N2} become much greater when f_{sp2} and f_{Na} rapidly increase. Moreover, when the load is applied along the [1 1 0] and [1 1 1] orientations, the decrease in f_{N1} becomes more evident with increasing R, indicating that more bond-breaking events would occur in a larger system (Fig. 4d–f).

The trends of f_{N1} and f_{N2} correspond well with the evolution of f_{Na}, which indicate that graphitization is highly dependent on the breaking of C–C bonds inside carbon tetrahedrons. When tetrahedrons are fully deformed, some of the intra-tetrahedron bonds break, leading to the transformation of the sp^3 bonding states into sp^2 bonding states. Therefore, broken intra-tetrahedron bonds induce the graphitization of T-carbon NWs and directly contribute toward the strain hardening effect (Fig. 5).

The breaking of intra-tetrahedron bonds can be further understood by evaluating the distribution of inter-tetrahedron bond angles before the onset of C–C bond-breaking in the carbon tetrahedron (Fig. 5a–c). The inter-tetrahedron bond angle α refers to the angle formed between an inter-tetrahedron and intra-tetrahedron bond. The α corresponding to the energy minima is calculated to be ~ 144.7° (Fig. 5d), which agrees well with its previously reported value of 144.74° in the equilibrium structure of T-carbon obtained using first principles calculations [18].

Each atom forms three intra-tetrahedron bonds with three other constituent carbon atoms and an inter-tetrahedron bond with an atom from another tetrahedron. Therefore, there are twelve inter-tetrahedron bond angles characterizing each carbon tetrahedron. The values of these twelve angles α angles before the onset of intra-tetrahedron bond-breaking are recorded for each tetrahedron. The largest of these twelve angles is taken as the representative angle θ (α_{max}), where θ ranges between 150 and 180°. We recorded the value of θ for each tetrahedron and constructed a distribution of the fraction f_{Nc}, defined as the ratio of the number of tetrahedrons that break at θ to the total number of tetrahedrons in the undeformed NW (Fig. 5a–c).

The f_{Nc} distributions under compression along the three lattice orientations are different from one another due to the anisotropy of the T-carbon NWs. The arrangement and distribution of regular tetrahedrons are inherently different along the three lattice orientations, which induce different deformation behaviors of the intra-tetrahedron bonds and changes to the graphitization process. Moreover, the deformation behaviors of α along different lattice orientations would vary from one another rather significantly.

As θ approaches the angle associated with the energy minima of the tetrahedron (144.7), the intra-tetrahedron bonds become more susceptible to breaking along [1 1 0] lattice orientation. For instance, when R increases from 35 to 65 Å, it can be seen that f_{Nc} shifts to the left (*i.e.*, the values of θ shift closer to 144.7). Accordingly, such a shift in the distribution of θ (Fig. 5a–c) correlates well with a dramatic increase in f_{N1} (Fig. 4d–f) and f_{sp2} (Fig. 2d–f). Therefore, the smaller the bond angle deviation is from its equilibrium value, the easier it is for intra-tetrahedron bonds to break and graphitization to occur along the [1 1 0] lattice orientation. In addition, for the [1 0 0] and [1 1 1] lattice orientations, the trend of θ does not change obviously, which is consistent with the final degree of graphitization.

To further confirm the effect of the inter-tetrahedron bond angle's

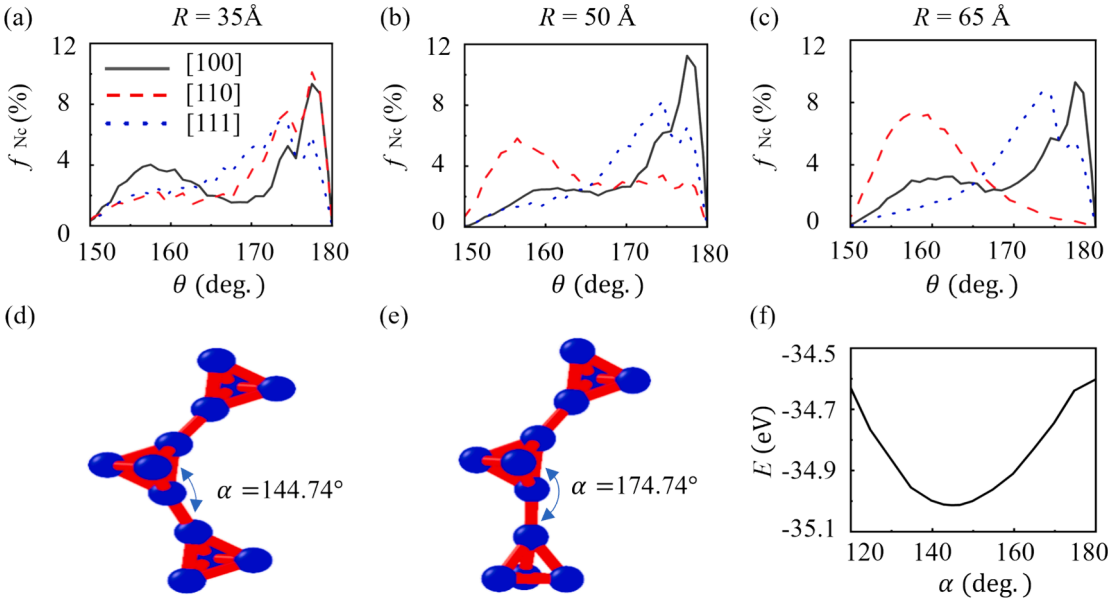

Fig. 5. (a)–(c) f_{Nc} distributions of T-carbon NWs under compression along different lattice orientations with R equal to 35, 50, and 65 Å, respectively. (d)–(e) The inter-tetrahedron bond angle α before and after deformation, respectively. (f) Variation of the total energy E with α for a prototypical system comprising three T-carbon tetrahedrons.

deformation on the breaking of intra-tetrahedron bonds, we built a prototypical system comprising three T-carbon tetrahedrons. We then adjusted the angle α between two tetrahedrons and calculated the system's total energy E (Fig. 5d–f). It is shown that E reaches its minima when α is 144.7°. As α increases from 144.7° to 180°, E increases significantly. The greater α deviates from the angle corresponding to the energy minima (144.7), the more energy is stored in the carbon tetrahedron. Accordingly, when θ lies closer to 144.7°, the amount of strain energy accumulated in the tetrahedron is smaller. Consequently, the tetrahedron is unable to store additional strain energy *via* deformation, and any excess strain energy imparted on the tetrahedron results in the breaking of its intra-tetrahedron bonds. To summarize, when θ tends toward the bond angle associated with the energy minima (144.7), the carbon tetrahedron can accommodate less strain energy *via* deformation, and any excess strain energy is discharged by breaking its intra-tetrahedron bonds, which promotes a higher degree of graphitization along [1 1 0] lattice orientation.

3.4. Strain hardening behavior in bulk T-carbon

In order to test whether the mechanism of strain hardening of T-carbon observed above is unique for the NWs, perhaps affected by size effects and buckling behavior, the compression tests are conducted on bulk T-carbon along the investigated lattice orientations, and the corresponding simulation results are shown in Fig. 6.

In addition, to verify that the mechanical strength of the newly formed sp^2-dominated network is stronger than that of the original sp^3-dominated network, we extract the sp^2-dominated carbon network from the T-carbon structure after deformation and investigate its mechanical properties (Fig. 6a). It is noted that we have also used hydrostatic compression and found that the governing deformation mechanism is not changed.

Similar to the T-carbon NWs, strain hardening is also observed in bulk T-carbon and is caused by graphitization. From Fig. 6a and b, it can be seen that a large increase in f_{sp2} causes a large drop in the value of σ in bulk T-carbon under compressive loading along all three lattice orientations. For example, when ε=~0.52, the value of f_{sp2} increases from 0 to 40 %, and σ decreases from 20 to 10 GPa for the [1 0 0] lattice orientation, which indicates that graphitization results in stress relaxation. It is worth mentioning that initially, graphitization occurs randomly in the bulk T-carbon. This occurs because the sp^2-bonding atoms are absent in the bulk structure, which can otherwise induce strain localization and nucleate the graphitization. Although the nucleation sites are different between the NWs and bulk structure, the graphitization mechanism and the resulting strain hardening behavior remain similar. Compared to the [1 0 0] orientation, the trend of σ in the other two lattice orientations are relatively smooth. This phenomenon is consistent with that observed in the case of NWs.

A comparison of Fig. 6b and c shows that graphitization is induced by breaking intra-tetrahedron bonds of bulk T-carbon. Similar to the T-carbon NWs, f_{N1} and f_{N2} change rapidly when f_{sp2} increase, indicating that graphitization is highly dependent on broken C–C bonds in the tetrahedrons. For example, when ε=~0.52, the value of f_{sp2} increases from 0 to 40 %, f_{N1} decreases from 100 to 88 %, and f_{N2} increases from 24 to 36 %. Again, this phenomenon is consistent with that observed in the case of NWs.

Moreover, the strength of bulk T-carbon is greatly enhanced after graphitization, which is attributed to the higher strength of the newly formed sp^2-dominated network. The strength of the sp^2-dominated network in T-carbon increases rapidly to 83 GPa when $\varepsilon < 0.45$, which is much higher than that of the original sp^3-dominated carbon network. These findings reconfirm that strain hardening stems from graphitization. For example, when the value of f_{sp2} increases as the strain surpasses 0.6, the value of σ increases rapidly from 9 to 99 GPa along the [1 0 0] orientation (Fig. 6a). Therefore, strain hardening caused by graphitization can endow T-carbon with impressive ductility under compressive strain.

Furthermore, the carbon tetrahedrons of bulk T-carbon have a strong ability to resist deformation. As shown in Fig. 6b, the value of f_{sp2} is 0 when $\varepsilon < 0.4$. This is because the structure of each carbon tetrahedron of bulk T-carbon remains intact, and the entire bulk material is a sp^3-hybridized carbon structure. Moreover, the carbon tetrahedrons of bulk T-carbon can absorb a large amount of strain energy through deformation, which leads to a high failure strain of the material.

Fig. 7 compares T-carbon's ultimate strength and density with those of various other carbon materials and some common metals. In order to highlight the effect of strain hardening in improving the strength of T-carbon, it is first compared with other carbon materials [14,36,49,56–60]. T-carbon has a lower density (1.27 g/cm^3) determined through MD than diamond, diamond-like carbon, M−carbon, and pentadiamond. Generally, the mechanical properties of carbon materials increase gradually with an increase in density [1,4]. However, the ultimate compressive strength of T-carbon (99 GPa) is 66 % of that of diamond-like carbon (150 GPa), while the density of T-carbon counts for only 43 %. In addition, as a porous carbon material, graphene aerogel, with a density (0.96 g/cm^3) lower than that of T-carbon, possesses an ultimate compressive strength (1.39 GPa) that is significantly lower than that of T-carbon.

Considering that T-carbon exhibits high ductility and strain hardening behavior similar to that of metals, the strength of T-carbon is also compared with that of various metals [61–64]. These metallic materials can be up to ~ 7 times denser than T-carbon, but T-carbon can be up to ~ 70 times stronger than some of them. Besides, compared to other materials such as polyethylene and SiC [65–67], T-carbon possesses a lower density, yet larger strength, which makes it an ideal candidate for lightweight devices. Since T-carbon exhibits synergistic qualities in terms of strength and ductility, it can be applied to devices with such requirements, such as in the field of aerospace [29]. Experiments have achieved the large-scale fabrication of T-carbon with precise control over its microstructure. We anticipate that the present findings could

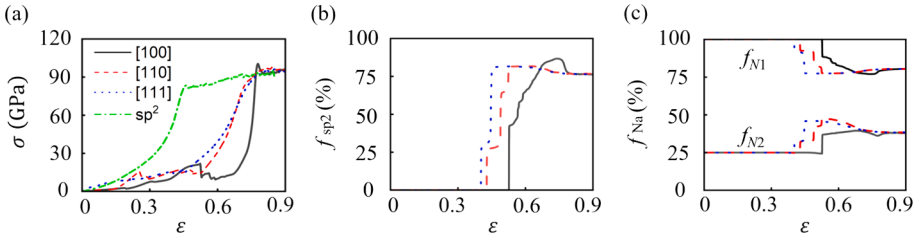

Fig. 6. Deformation behavior of bulk T-carbon. (a) Stress–strain curves of bulk T-carbon with compressive loading applied along different lattice orientations. "sp^2" denotes the stress–strain curve of the newly formed sp^2-dominated carbon network with compressive loading applied along the [1 0 0] lattice orientation. (b) Evolution of f_{sp2} in bulk T-carbon with compressive loading applied along different lattice orientations. (c) Evolution of f_{Nb} in bulk T-carbon with compressive loading applied along different lattice orientations.

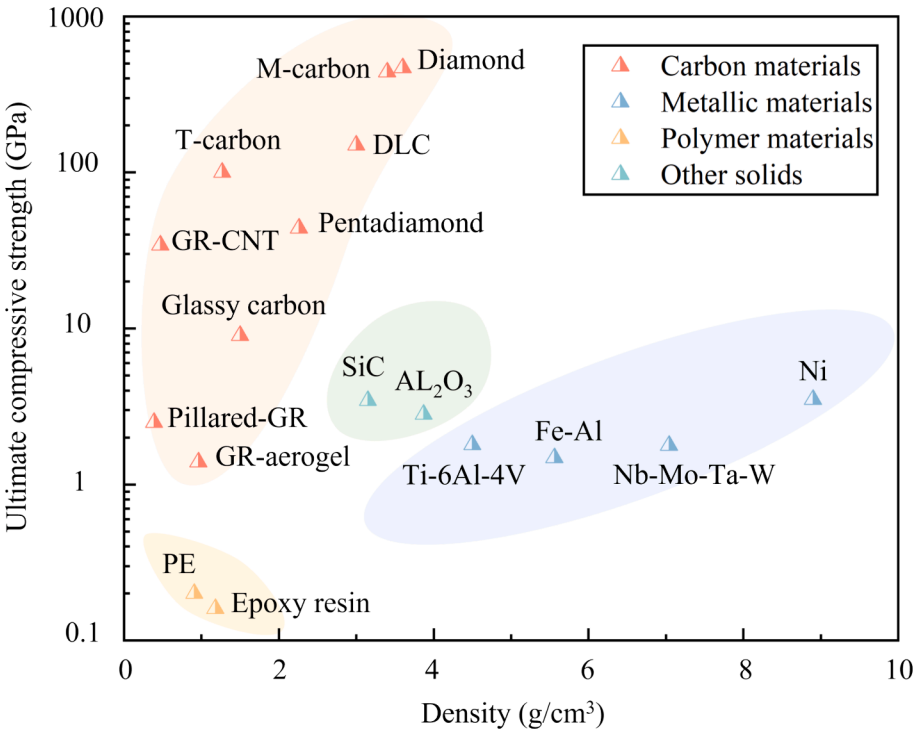

Fig. 7. Comparison of the ultimate strengths of various materials with different densities (DLC: diamond-like carbon, GR-CNT: three-dimensional graphene carbon nanotube, GR-aerogel: three-dimensional graphene aerogel, Pillared-GR: three-dimensional pillared graphene, PE: polyethylene).

facilitate the engineering design of T-carbon with desired mechanical properties and shed light on its application prospects.

4. Conclusions

The implications of strain hardening on the mechanical performance and deformation mechanisms of T-carbon under compressive loading are investigated using molecular dynamic simulations.

Strain hardening can improve the strength–ductility synergy of T-carbon. It is found that strain hardening manifests due to a transformation from the original sp^3-dominated network to a graphitized sp^2-network, during which more strain energy is stored in the sp^2-network. This newly formed network can afford a higher compressive strain and lead to excellent mechanical strength under plastic deformation. In addition, with the increase in the cross-sectional radius of the T-carbon nanowires, graphitization propagation in T-carbon nanowires is most pronounced along the [1 1 0] lattice orientation, while it shows lower sensitivity in the [1 0 0] orientation.

Graphitization in T-carbon nanowires is dominated by the deformation behavior of the inter-tetrahedron bond angles, which induce thefracture of tetrahedrons. The closer the largest inter-tetrahedron bond angle is to its equilibrium value, the easier it is for graphitization to proceed along the [1 1 0] lattice orientation. When the largest inter-tetrahedron bond angle approaches its value at equilibrium (144.74), less strain energy can be stored by the tetrahedron. Upon deformation, part of the strain energy is stored through the deformation of inter-tetrahedron bond angles, while the remaining strain energy induces the breaking of intra-tetrahedron bonds, thus activating the graphitization process.

The underlying mechanisms behind strain hardening and graphitization are also found to occur in the bulk T-carbon structure. Furthermore, the mechanisms revealed in this work provide an impetus for new strategies to design high-strength, high-ductility, and low-density carbon structures.

CRediT authorship contribution statement

Runhua Zhou: Writing – original draft, Software, Methodology, Investigation, Formal analysis, Data curation, Conceptualization. **Lichun Bai:** Methodology, Formal analysis. **Changjin Huang:** Writing – review & editing. **Narasimalu Srikanth:** Writing – review & editing, Funding acquisition, Project administration. **Mao See Wu:** Writing – review & editing, Supervision.

Declaration of competing interest

The authors declare that they have no known competing financial interests or personal relationships that could have appeared to influence the work reported in this paper.

Data availability

Data will be made available on request.

Acknowledgement

The computational work for this article was performed using resources of the Singapore National Supercomputing center. Dr. Narasimalu Srikanth wishes to thank National Research Foundation (NRF), Maritime Port Authority (MPA) & Singapore Maritime Institute (SMI) for funding the project (NRF-000263-00), which contributed to this research.

References

[1] Y. Yang, Z. Song, G. Lu, Q. Zhang, B. Zhang, B. Ni, et al., Intrinsic toughening and stable crack propagation in hexagonal boron nitride, Nature 594 (7861) (2021) 57–61.
[2] H. Wu, M. Huang, Y. Xia, X. Li, R. Li, C. Liu, et al., The importance of interfacial stress-affected zone in evading the strength-ductility trade-off of heterogeneous multi-layered composites, Int. J. Plast. 160 (2023) 103485.

[3] H. Wu, G. Fan, An overview of tailoring strain delocalization for strength-ductility synergy, Prog. Mater. Sci 113 (2020) 100675.
[4] X. Xue, P. Wang, M. Gong, J. Tian, Y. Qiao, J. Shan, et al., Time-dependent microstructural evolution mechanisms of twisted carbon nanotube fibers under tension and relaxation, Int. J. Plast. 136 (2021) 102866.
[5] H. Liu, X. Shang, B. He, Z. Liang, Strain rate dependence of strengthening mechanisms in ultrahigh strength lath martensite, Int. J. Plast. 161 (2023) 103495.
[6] P. Shi, R. Li, Y. Li, Y. Wen, Y. Zhong, W. Ren, et al., Hierarchical crack buffering triples ductility in eutectic herringbone high-entropy alloys, Science 373 (6557) (2021) 912–918.
[7] H. Li, H. Zong, S. Li, S. Jin, Y. Chen, M.J. Cabral, et al., Uniting tensile ductility with ultrahigh strength via composition undulation, Nature 604 (7905) (2022) 273–279.
[8] Y. Sun, X. Kong, Z. Wang, Superior mechanical properties and deformation mechanisms of a 304 stainless steel plate with gradient nanostructure, Int. J. Plast. 155 (2022) 103336.
[9] Q. Pan, L. Zhang, R. Feng, Q. Lu, K. An, A.C. Chuang, et al., Gradient cell–structured high-entropy alloy with exceptional strength and ductility, Science 374 (6570) (2021) 984–989.
[10] M. Hazarabedian, N. Haghdadi, S. Primig, M. Lison-Pick, M. Quadir, M. Ferry, et al., Formation of intergranular phases in precipitation hardening nickel-based alloy 725, Acta Mater. 236 (2022) 118108.
[11] S. Qin, M. Yang, P. Jiang, J. Wang, X. Wu, H. Zhou, et al., Designing structures with combined gradients of grain size and precipitation in high entropy alloys for simultaneous improvement of strength and ductility, Acta Mater. 230 (2022) 117847.
[12] G. Sun, X. Feng, X. Wu, S. Zhang, B. Wen, Is hardness constant in covalent materials? J. Mater. Sci. Technol. 114 (2022) 215–221.
[13] Z. Zhu, C. Jiang, C. Chen, S. Lu, M. Jiang, X. Li, et al., Ordinary-pressure phase transition from graphite to diamond induced by monodispersed Ta atoms, Carbon 118098 (2023).
[14] Y. Yu, X. Zhang, S. Yin, L. Bai, Z. Liu, The sp^2-sp^3 transition and shear slipping dominating the compressive deformation of diamond-like carbon, J. Non-Cryst. Solids 577 (2022) 121318.
[15] C. Wang, H. Huang, Y. Qian, Z. Zhang, J. Yan, One-step fabrication of regular hierarchical micro/nano-structures on glassy carbon by nanosecond pulsed laser irradiation, J. Manuf. Process. 62 (2021) 108–118.
[16] K. Wu, Q. Zhou, J. Cao, Z. Qian, B. Niu, D. Long, Ultrahigh-strength carbon aerogels for high temperature thermal insulation, J. Colloid Interface Sci. 609 (2022) 667–675.
[17] S. Zhu, S. Peng, Z. Qiang, C. Ye, M. Zhu, Cryogenic-environment resistant, highly elastic hybrid carbon foams for pressure sensing and electromagnetic interference shielding, Carbon 193 (2022) 258–271.
[18] X.-L. Sheng, Q.-B. Yan, F. Ye, Q.-R. Zheng, G. Su, T-carbon: a novel carbon allotrope, Phys. Rev. Lett. 106 (15) (2011) 155703.
[19] J. Zhang, R. Wang, X. Zhu, A. Pan, C. Han, X. Li, et al., Pseudo-topotactic conversion of carbon nanotubes to T-carbon nanowires under picosecond laser irradiation in methanol, Nat. Commun. 8 (1) (2017) 683.
[20] K. Xu, H. Liu, Y.-C. Shi, J.-Y. You, X.-Y. Ma, H.-J. Cui, et al., Preparation of T-carbon by plasma enhanced chemical vapor deposition, Carbon 157 (2020) 270–276.
[21] J. Feng, C. Yang, L. Zhang, F. Lai, L. Du, X. Yang, First-principle calculation of distorted T-carbon as a promising anode for Li-ion batteries with enhanced capacity, reversibility, and ion migration properties, Carbon Energy 2 (4) (2020) 614–623.
[22] L.-R. Cheng, Z.-Z. Lin, X.-M. Li, X. Chen, Can T-carbon serve as a Li storage material and a Li battery anode? Mater. Adv. 2 (14) (2021) 4694–4701.
[23] Z.-W. Tian, X.-Q. Cui, J.-K. Tian, M.-C. Cui, L. Jin, R. Jia, et al., Co-doping with boron and nitrogen impurities in T-carbon, J. Saudi Chem. Soc. 24 (11) (2020) 857–864.
[24] Z. Zhao, J. Hao, B. Jia, X. Zhang, G. Wu, C. Zhang, et al., Transition metal embedded in nonmetal-doped T-carbon [110]: A superior synergistic trifunctional electrocatalyst for HER, OER and ORR, J. Energy Chem. 83 (2023) 79–89.
[25] S. Li, X. Xu, M. Zhang, W. Hu, J. Tang, Y. Shi, et al., Facile preparation of OHB-T–carbon nanotube composite films for modification of the electrical and optical properties, Appl. Phys. A. 129 (6) (2023) 441.
[26] Y. Cao, C. Zhang, Y. Liu, B.-S. Li, Z.G. Yu, Y.-W. Zhang, Irradiation-induced defects and their effects on the electronic structures in T-carbon, J. Phys. Chem. C. 125 (51) (2021) 28067–28074.
[27] J.-Y. You, X.-L. Sheng, G. Su, Topological gimbal phonons in T-carbon, Phys. Rev. B 103 (16) (2021) 165143.
[28] J.-Y. You, B. Gu, G. Su, Superconductivity in sodium-doped T-carbon, Phys. Rev. B 101 (18) (2020) 184521.
[29] X.-W. Yi, Z. Zhang, Z.-W. Liao, X.-J. Dong, J.-Y. You, G. Su, T-carbon: Experiments, properties, potential applications and derivatives, Nano Today 42 (2022) 101346.
[30] H. Rafii-Tabar, Computational modelling of thermo-mechanical and transport properties of carbon nanotubes, Phys. Rep. 390 (4–5) (2004) 235–452.
[31] S. Plimpton, Fast parallel algorithms for short-range molecular dynamics, J. Comput. Phys. 117 (1) (1995) 1–19.
[32] B. Yin, J. Huang, W. Ji, K. Liew, Exploring frictional performance of diamond nanothread reinforced polymer composites from the atomistic simulation and density functional theory, Carbon 200 (2022) 10–20.
[33] A. Pedrielli, S. Taioli, G. Garberoglio, N.M. Pugno, Designing graphene based nanofoams with nonlinear auxetic and anisotropic mechanical properties under tension or compression, Carbon 111 (2017) 796–806.
[34] L. Bai, P.-P. Sun, B. Liu, Z. Liu, K. Zhou, Mechanical behaviors of T-carbon: A molecular dynamics study, Carbon 138 (2018) 357–362.
[35] X. Shi, X. He, L. Wang, L. Sun, Hierarchical-structure induced adjustable deformation of super carbon nanotubes with radial shrinkage up to 66%, Carbon 125 (2017) 289–298.
[36] X. Liu, P. Yu, C. Lu, Mechanical property and thermal conductivity of pentadiamond: A comprehensive molecular dynamics study, Comput. Mater. Sci. 203 (2022) 111039.
[37] A. Stukowski, Visualization and analysis of atomistic simulation data with OVITO–the Open Visualization Tool, Model. Simul. Mater. Sci. Eng. 18 (1) (2009) 015012.
[38] Y. Fu, J. Wu, S. Xiao, S. Liu, Z. Zhang, J. He, Tensile mechanical characteristics of ultra-thin carbon sulfur nanothreads in orientational order, Carbon 184 (2021) 146–155.
[39] Z. Yin, Y. Yu, H. Chen, J. Li, L. Bai, Nanofriction behaviors between silicon-doped diamond-like carbon films under different testing conditions, Comput. Mater. Sci. 188 (2021) 110182.
[40] H. Matsubara, G. Kikugawa, T. Bessho, T. Ohara, Evaluation of thermal conductivity and its structural dependence of a single nanodiamond using molecular dynamics simulation, Diam. Relat. Mater. 102 (2020) 107669.
[41] C. Qiu, Y. Su, J. Yang, X. Wang, B. Chen, Q. Ouyang, et al., Microstructural characteristics and mechanical behavior of SiC (CNT)/Al multiphase interfacial micro-zones via molecular dynamics simulations, Compos. B: Eng. 220 (2021) 108996.
[42] P.K. Sarkar, N. Mitra, Molecular level study of uni/multi-axial deformation response of tobermorite 11 Å: A force field comparison study, Cem. Concr. Res. 145 (2021) 106451.
[43] W. Ji, M.S. Wu, Nanoscale origin of the crystalline-to-amorphous phase transformation and damage tolerance of Cantor alloys at cryogenic temperatures, Acta Mater. 226 (2022) 117639.
[44] M. Chen, S. Quek, Z. Sha, C. Chiu, Q. Pei, Y. Zhang, Effects of grain size, temperature and strain rate on the mechanical properties of polycrystalline graphene–A molecular dynamics study, Carbon 85 (2015) 135–146.
[45] J. Guo, B. Wen, R. Melnik, S. Yao, T. Li, Molecular dynamics study on diamond nanowires mechanical properties: Strain rate, temperature and size dependent effects, Diam. Relat. Mater. 20 (4) (2011) 551–555.
[46] J.M. Wheeler, R. Raghavan, J. Wehrs, Y. Zhang, R. Erni, J. Michler, Approaching the limits of strength: measuring the uniaxial compressive strength of diamond at small scales, Nano Lett. 16 (1) (2016) 812–816.
[47] Z. Hu, X. Fan, C. Chen, Multiscale frictional behaviors of sp^2 nanocrystallited carbon films with different ion irradiation densities, Friction 9 (2021) 1025–1037.
[48] D. Shin, D. Jang, Crack-tip plasticity and intrinsic toughening in nano-sized brittle amorphous carbon, Int. J. Plast. 127 (2020) 102642.
[49] Z. Qin, G.S. Jung, M.J. Kang, M.J. Buehler, The mechanics and design of a lightweight three-dimensional graphene assembly, Sci. Adv. 3 (1) (2017) e1601536.
[50] D. Zhao, B. Zhu, S. Wang, Y. Niu, L. Xu, H. Zhao, Effects of pre-strain on the nanoindentation behaviors of metallic glass studied by molecular dynamics simulations, Comput. Mater. Sci. 186 (2021) 110073.
[51] F. Shuang, K.E. Aifantis, Modelling dislocation-graphene interactions in a BCC Fe matrix by molecular dynamics simulations and gradient plasticity theory, Appl. Surf. Sci. 535 (2021) 147602.
[52] G. Qin, K.-R. Hao, Q.-B. Yan, M. Hu, G. Su, Exploring T-carbon for energy applications, Nanoscale 11 (13) (2019) 5798–5806.
[53] Z. Yao, Y. Yuan, T. Cheng, L. Gao, T. Sun, Y. Lu, et al., Anomalous size effect of Pt ultrathin nanowires on oxygen reduction reaction, Nano Lett. 21 (21) (2021) 9354–9360.
[54] J. Yan, S. Yin, M. Asta, R.O. Ritchie, J. Ding, Q. Yu, Anomalous size effect on yield strength enabled by compositional heterogeneity in high-entropy alloy nanoparticles, Nat. Commun. 13 (1) (2022) 2789.
[55] L. Bai, N. Srikanth, H. Wu, Y. Liu, B. Liu, K. Zhou, Investigation on tensile behaviors of diamond-like carbon films, J. Non-Cryst. Solids 443 (2016) 8–16.
[56] M. Hu, J. He, Z. Zhao, T.A. Strobel, W. Hu, D. Yu, et al., Compressed glassy carbon: An ultrastrong and elastic interpenetrating graphene network, Sci. Adv. 3 (6) (2017) e1603213.
[57] F. Liu, R. Zou, N. Hu, H. Ning, C. Yan, Y. Liu, et al., Understanding the mechanical properties and deformation behavior of 3-D graphene-carbon nanotube structures, Mater. Des. 160 (2018) 377–383.
[58] Y. Wang, Y. Zhu, F. Wang, X. Liu, H. Wu, Super-elasticity and deformation mechanism of three-dimensional pillared graphene network structures, Carbon 118 (2017) 588–596.
[59] B. Xu, Y. Tian, Ultrahardness: measurement and enhancement, J. Phys. Chem. C. 119 (10) (2015) 5633–5638.
[60] X. Luo, Z. Liu, B. Xu, D. Yu, Y. Tian, H.-T. Wang, et al., Compressive strength of diamond from first-principles calculation, J. Phys. Chem. C. 114 (41) (2010) 17851–17853.
[61] J. Xu, R. Duan, K. Feng, C. Zhang, Q. Zhou, P. Liu, et al., Enhanced strength and ductility of laser powder bed fused NbMoTaW refractory high-entropy alloy via carbon microalloying, Addit. Manuf. Lett. 3 (2022) 100079.
[62] Y. Liu, J. Meng, L. Zhu, H. Chen, Z. Li, S. Li, et al., Dynamic compressive properties and underlying failure mechanisms of selective laser melted Ti-6Al-4V alloy under high temperature and strain rate conditions, Addit. Manuf. 54 (2022) 102772.
[63] G.M. Valentino, S. Xiang, L. Ma, K.Y. Xie, M.-R. He, W.C. Oliver, et al., Hemker, Investigating the compressive strength and strain localization of nanotwinned nickel alloys, Acta Mater. 204 (2021) 116507.

[64] Y. Bai, J. Zhou, J. Li, Z. Yang, B2-ordered NiAl content on microstructure, mechanical and oxidation properties of FeAl intermetallic compounds, J. Mater. Res. Technol. 16 (2022) 1875–1888.
[65] C. Li, Y. Zhou, H. Zhan, J. Bai, Y. Gu, Effective enhancement of a carbon nanothread on the mechanical properties of the polyethylene nanocomposite, J. Phys. Chem. C 125 (10) (2021) 5781–5792.
[66] P. Wang, S. Zhong, K. Yan, B. Liao, J. Zhang, Influence of a batch of hollow glass microspheres with different strength grades on the compression strength of syntactic foam, Compos. Sci. Technol. 223 (2022) 109442.
[67] Q. Zhang, Y. Zheng, F. Zhou, T. Yu, Fragmentations of Alumina (Al2O3) and Silicon Carbide (SiC) under quasi-static compression, Int. J. Mech. Sci. 167 (2020) 105119.